Computational Materials Science 98 (2015) 142–148

Contents lists available at ScienceDirect

Computational Materials Science

journal homepage: www.elsevier.com/locate/commatsci

Atomistic modeling of Ag, Au, and Pt nanoframes

Silvina E. Fioressi [a,b], Daniel E. Bacelo [a,b], Guillermo Bozzolo [c,*], Hugo O. Mosca [d,e], Mariela F. del Grosso [b,d,f]

[a] Departamento de Química, Facultad de Ciencias Exactas y Naturales, Universidad de Belgrano, Villanueva 1324 CP 1426, Buenos Aires, Argentina
[b] Consejo Nacional de Investigaciones Científicas y Técnicas, Buenos Aires, Argentina
[c] Loyola University of Maryland, 4501 N. Charles St, Baltimore, MD 21210, USA
[d] Grupo de Caracterización y Modelación de Materiales, UTN, FRGP, H. Yrigoyen 288, B1617FRP Gral. Pacheco, Argentina
[e] Materia Condensada, Gerencia de Investigación y Aplicaciones, Comisión Nacional de Energía Atómica, Av. Gral. Paz 1499, B1650KNA San Martín, Argentina
[f] Sub-Gcia. de Tecnología y Aplicaciones de Aceleradores – Comisión Nacional de Energía Atómica, Av. Gral. Paz 1499, B1650KNA San Martín, Argentina

ARTICLE INFO

Article history:
Received 10 July 2014
Received in revised form 31 October 2014
Accepted 4 November 2014

Keywords:
BFS method
Nanoframes
Metallic nanocages

ABSTRACT

Cubic monoatomic nanoframes of Ag, Au, and Pt were modeled in terms of their evolution with temperature. Using an approximate quantum method for the energetics, Monte Carlo atomistic simulations were performed to determine the critical temperatures at which the nanoframe evolves from its original shape to either a cluster of nanoparticles after all sides of the frame are broken, or to a large cluster after collapsing onto its own internal void. The mechanisms by which these two behaviors take place are discussed within the framework of a simple rule which determines the relationship between the structural factors (side and width) that characterize the transition from one to the other.

1. Introduction

Considerable research efforts are being made in the development of nanoparticles with hollow interiors and specific external structure (both in shape and composition) [1–5]. Their physical and optical properties seem to be a consequence of such particular atomic distributions [6], leading to remarkable catalytic properties [7–9] and a wide range of possible applications in the medical field [10]. Such is the case for gold nanocages which, due to their biocompatibility, have been the subject of numerous studies for their application in photothermal therapy, cancer cell imaging, and radiotherapy [11–16].

Hollow nanostructures of noble metals have been effectively prepared through the galvanic replacement reaction developed by Sun and Xia [17]. Special efforts were made to determine means to meet desired requirements in terms of their shape and size, as well as porosity, resulting in specific optical properties. The most successful approach is to prepare Ag nanostructures with the desired size and shape as a template, and then replace the Ag atoms with a less reactive metal such Au, Pd, or Pt [18–22]. The Ag templates can be easily synthesized by reducing $AgNO_3$ with ethylene glycol in the presence of poly(vinylpyrrolidone) which serves as a protective coating for the metallic nanocubes. The reactants proportions, reaction times and temperature in this so called polyol method [17], are crucial to control the size of the Ag nanostructures formed, ranging from 20 nm to 250 nm [22]. For example, Lu et al. [18] fabricated Au nanocages with controlled wall thickness and porosity by dealloying Ag/Au nanocubes with $Fe(NO_3)_3$ or NH_4OH. Recently, preparation of Pt and Pd nanocages with outstanding electrocatalytic activities has been reported by Wu and co-workers, achieving size and shape control by modifying the sizes of Ag nanocube templates and their reaction temperatures [23].

Thermal behavior of nanoframes is important not only from the point of view of synthesis, but also for application purposes. In drug delivery applications, drugs hold and release is regulated through light-induced temperature changes [24]. The interaction of light with the nanocages results in an increase in temperature as absorbed photons induce vibrations in the lattice, and therefore changing their overall structure [25,26]. Chen et al. demonstrated that exposing Au nanocages to a flash camera can increase the local temperature beyond their melting point, transforming the nanocages into almost spherical nanoparticles [25]. Due to the interest in biomedical processes, it is necessary to avoid reaching the melting point of the metallic nanocages, and instead restrict the local increase in temperature to the point where only targeted cancer cells are affected. Such photothermal therapy could constitute a novel treatment for cancer, as an alternative to the much more aggressive traditional chemotherapy.

The catalytic efficiency of noble metals nanostructures is strongly dependent on the size and composition of the nanocage.

---

* Corresponding author.
E-mail address: guille_bozzolo@yahoo.com (G. Bozzolo).

http://dx.doi.org/10.1016/j.commatsci.2014.11.003
0927-0256/

Such correlation was the subject of the work by Mahmoud et al. [27]. In their work, it was found that the catalysis takes place in the nanocage cavity, effectively acting as a nanoreactor. In addition, the study by Zhang et al. on the catalyzed oxidation of CO in excess hydrogen shows an increase in catalytic efficiency for smaller nanocages, which are expected to be more fragile than bigger ones [28]. Many catalyzed reactions are carried out at relatively high temperatures, suggesting that the thermal stability of nanocages is an important feature to take into account.

However, while there is some agreement on how to develop nanostructures with specific characteristics (size, thickness, composition, etc.), most of the current knowledge is based mostly on experimental evidence [1–28]. The general lack of basic information on the properties of such structures, even ideal ones, could limit their applicability, as few features, either desirable or not, can be controlled during the formation process. Relevant theoretical and modeling work has been done on structures that are related to those described in this article [29–36]. Atomistic simulations of nanotubes and spheres [30,31] and nanocages [32,33] have shown how their mechanical and structural properties are dependent on their size, shape and wall thickness. The effect of increasing temperature on the nanostructures properties and atomic distribution was studied mainly through molecular dynamics simulations [30–36]. In most cases, the temperatures at which the structure collapses were found to be lower than the melting temperature of the corresponding bulk material. This paper aims at adding to the current body of work by addressing these basic issues for the specific case of cubic nanoframes, providing some fundamental hints on what to avoid and what to look for in the process of nanoframe formation, in terms of their stability as a function of temperature and original dimensions [30,31].

Therefore, a systematic study of several monoatomic nanoframes based on atomistic simulations was performed, where atomic interactions were modeled by means of the Bozzolo–Ferrante–Smith (BFS) method for alloys [37,38]. This approach has been successfully implemented for a number of cases dealing with nanoparticles, as well as nanoscale properties in alloy systems with several elements [39–44], raising the necessary confidence for the current application to nanocages. Previous studies include the multiphase nanostructure formation in a 5-element Ni–Al–Ti–Cr–Cu alloy [39] as well as surface alloying and the nanoscale formation Co–Cu surface patterns on a Cu(1 1 1) surface [40]. In a recent study [41], the method was used to simulate the diffusion-driven carbon nanotube growth and their structural stability. In agreement with experiment, the study highlights the relevance of the order of deposition of a binary catalyst layer, thus showing that the BFS-based methodology constitutes an appropriate tool for studying catalyst particles and their relevance in the growth of carbon nanotubes. A study by Negreiros Ribeiro et al. [42] focused on the formation of Ag–Au nanoparticles, using the method for studying the formation process, and shedding light on the competing processes resulting in a specific final shape, size, and structure. They also showed how the relative relevance of each process depends on the participating elements and their relative proportions, obtaining as a result an excellent agreement with experiment. Other BFS-based studies include ordering and segregation properties in Fe–Pt nanoparticles [43] and the formation of nanowires on stepped surfaces [44].

As demonstrated in Refs. [29–36], similar detailed modeling of hollow nanostructures may be performed with other theoretical and numerical approaches. However, their reliance on a limited number of available potentials and/or parameters, limits their application to multicomponent systems with two or more arbitrary elements, a limitation which, as discussed above, makes their analysis with other techniques less feasible as the complexity of the system increases, but that may be easily avoided by using the BFS method. Based on this extensive background, it can be assumed that the BFS method is an appropriate technique for the study and development of nanostructures with specific characteristics. For the particular case of nanoframes, the method may prove to be useful for obtaining basic information on their formation process and thermal stability.

Although the simple structures described in this paper may be readily described by alternative techniques, the intention to extend this work to more complex systems warrants, from the beginning, the use of BFS, due to its lack of limitations on the number and type of elements [29–36].

2. Methodology

The BFS method [37,38] is a physically sound and computationally efficient technique for addressing issues that usually fall outside the realm of other modeling techniques, such as multicomponent systems and structures with low symmetry [39–44]. Its simplicity is mainly due to the underlying concept that individual atoms contribute to the total energy of the system separately. Further simplification is achieved by splitting the energy contribution of each individual atom into two unrelated components describing structural and chemical features, respectively. These two components are then linked by a coupling function in order to restore the equivalency between the modeled process and the actual process of alloy formation. As a result, the net contribution of each individual atom i to the total energy of formation can be written as

$$\varepsilon_i = \varepsilon_i^S + g_i\left(\varepsilon_i^C - \varepsilon_i^{C_0}\right) \qquad (1)$$

The computation of the strain energy contribution, ε_i^S, which accounts solely for structural effects, is done with Equivalent Crystal Theory [45], which relies on three single-element properties: the cohesive energy (E_c), the equilibrium lattice parameter (a), and the bulk modulus (B_0). The chemical energy contribution, ε_i^C, describes the effects of mixed composition, and it is treated as a defect in an otherwise monoatomic crystal. As it deals with pairs of atoms of different species, it relies on two parameters (perturbation on the otherwise monoatomic equilibrium electron density), Δ_{AB} and Δ_{BA}, which describe changes in the electron density between them due to the different chemical species. To avoid the introduction of structural effects in the chemical energy term, a reference chemical energy, $\varepsilon_i^{C_0}$, is included. Both terms, strain and chemical energies, are finally linked by a coupling function, g_i, so that the appropriate volume dependence and the resulting weight of the chemical contribution is taken into account. The single-element parameters may be obtained from theory as well as from experiment. The chemical interaction parameters, however, can only be determined by means of first-principles calculations. For this work, all parameters (including the single-element parameters) were computed using the Linearized Augmented Plane Wave method [46]. This was done by computing the zero temperature equation of state for each one of the individual pure solids (for the determination of the cohesive energy, lattice parameter, and bulk modulus), and by computing the energy of formation of fcc-based Ag–Au, Ag–Pt and Au–Pt bulk alloys as a function of volume (for the determination of the interaction parameters, even though they are not needed for this work). It should be noted, however, that in the initial phase of this study of nanocages, only the single-element parameters are needed, as all nanocages are monoatomic. As a result, the chemical component of the total energy is zero, making the total energy of the system equal to the strain energy component. Details on the BFS method, the calculation, meaning, and role of each parameter, and the general procedure for implementing the method to specific applications, can be found in previous BFS studies of multicomponent and nanoscale systems [39–44].

In all cases, the simulations started at $T = 0$ K with a rigid monoatomic cubic nanoframe with N atoms on each side, varying the width W, where W is defined as the number of parallel planes of a fcc lattice, as shown in Fig. 1. Given the chosen (100) orientation of the cells, $W = 1$ corresponds to a side width of half a lattice parameter, while $W = N$ would then describe a bulk solid cube. Being that the lowest surface energy orientation for fcc surfaces is (111), choosing the (100) plane as a cutoff plane ensures that all surface sites are energetically high, thus ensuring visible reaccommodation of all surface atoms. The initial lattice parameters were 0.4086 nm for Ag, 0.4068 nm for Au and 0.392 nm for Pt.

Each cell was then subjected to a simulation cycle of steadily increasing temperatures up to approximately the melting temperature (T_m) of the bulk crystal, from $T = 0$ to $T = 1400$ K (for Ag and Au, with $T_m = 1235$ K and 1337 K, respectively) and up to $T = 1900$ K (for Pt, with $T_m = 2045$ K). At each temperature cycle, the lowest total energy state was then taken as the initial state for the next temperature cycle. The cell, forced to retain the fcc symmetry, was allowed to breathe (i.e., isotropic compression or expansion) until the optimum (uniform) lattice parameter was determined.

Two simulation algorithms were used in each case, as in previous applications of BFS to other systems [39–44,47,48]. The first is the traditional Monte Carlo–Metropolis method, heretofore referred to as MCAS, as in Ref. [47], where all possible exchanges between atomic sites are considered. Whether they are accepted or not, depends on a probabilistic factor $e^{-\frac{\Delta E}{kT}}$, where ΔE is the change in energy before and after the exchange. The atomic distribution obtained at the end of each temperature step is consistent with results that would be obtained with infinite annealing time, as all types of atomic exchanges are considered. This approach yields accurate results in terms of what the lowest energy state is, but inaccurate in terms of comparison with experiment. It is appropriate, however, to describe the underlying trends of the system in the sense of what final distribution is most likely for a given atomic configuration.

For the purpose of this work, where simulations are only meant to illustrate and expand on the results obtained from the spectral analysis, it is convenient to introduce an alternative approach to aid in the understanding and interpretation of some features that characterize the results of the standard Monte Carlo–Metropolis procedure. While traditionally used for the determination of ground state properties, the MCAS approach does not necessarily provide the best means for comparison with experiment, due to its unrealistic treatment of atomic interdiffusion. The unlimited range of the atomic exchanges allows for ordering at very high temperatures, thus proving highly inefficient for a proper analysis of order–disorder transitions or any other structural change.

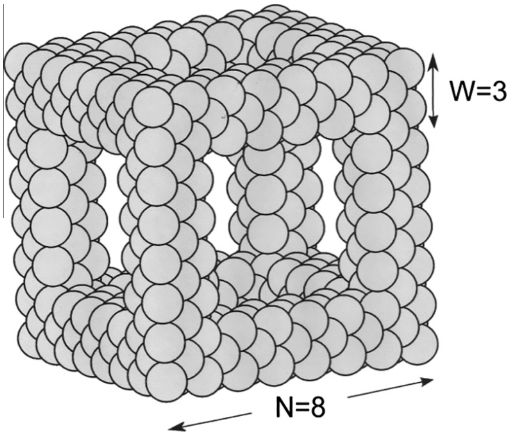

Fig. 1. Sketch of the computational cell for $N = 8$ and $W = 3$.

These limitations can be avoided, within the framework of an approximate variation of the standard Monte Carlo–Metropolis algorithm, solely designed to focus on the modeling of the low temperature behavior of individual atoms. A second simulation approach is therefore implemented, particularly designed to avoid these limitations. In this algorithm, which we denote BANN [47], we limit the range of atomic exchanges to pairs of atoms located at nearest-neighbor sites (NN). Moreover, we modify the probability criterion by defining it in terms of the ratio between the energy necessary for the exchange, ΔE, and the available thermal energy.

In this approach, the actual ground state of the system is not necessarily reached, as different atoms could eventually get 'trapped' at low temperatures, thus unable to reach their true equilibrium positions. Together, MCAS and BANN simulations supplement each other, providing insight not only on the nature of the thermodynamic ground state (MCAS) but also on the most likely features observed experimentally (BANN). We stress, however, that the BANN approach does not rely on a rigorous statistical mechanics foundation as MCAS does. It is, at best, a simple but approximate way to model the evolution of the system and therefore illustrate the consequences of the basic features of the energy spectrum that is obtained from the analytical calculations (i.e., small energy gaps between the low-lying energy levels). Besides the obvious benefit of visualizing the resulting atomic distribution, the results of either type of simulation, MCAS or BANN, provide useful information regarding the distribution of bonds in the final state.

3. Results and discussion

The BFS method was applied to the study of monoatomic cubic nanoframes of Ag, Au, and Pt. Being all monoatomic systems, the only relevant quantity is then the strain energy. As a representative example, Fig. 2 shows the BANN results for the evolution of the strain (total) energy with temperature for the $N = 10$ case and for several values or W, for pure Ag nanoframes. At low temperatures (generally below room temperature) all curves are relatively flat. Any fluctuations present in that temperature range are due to a very small number of atoms that migrate along the surface to high surface energy points, such as the corners of the cell, where atoms with the lowest coordination are located. This process of surface diffusion kicks off in earnest as the temperature increases, triggering changes in the shape of the nanoframe for temperatures ever closer to room temperature, as the width W increases.

In what follows, the example $N = 10$ (Ag) is again used as a reference for the discussion. It is reasonable to expect a distinction in the evolution of the nanoframes for cases with small or large values of W, for a given value of N. For small values of W, most atoms on the sides are surface atoms. Their migration should be favored with increasing temperature, leading to diffusion to the corners, which in turn would rearrange themselves in order to alleviate the high energy corner and edge sites, inducing the formation of small patches of low surface energy (111) planes. As a result, the sides would debilitate and tend to break and the corners would adopt a more bulk-like nature, with enough faceting so as to resemble small individual nanoclusters.

For $W = 2$, the breakdown of the sides is nearly complete by $T = 800$ K. For higher temperatures, any reduction in energy is due to faceting in the corners which have now partitioned into individual nanoclusters. Due to the small size of these clusters (392 atoms), it is reasonable to expect the melting temperature

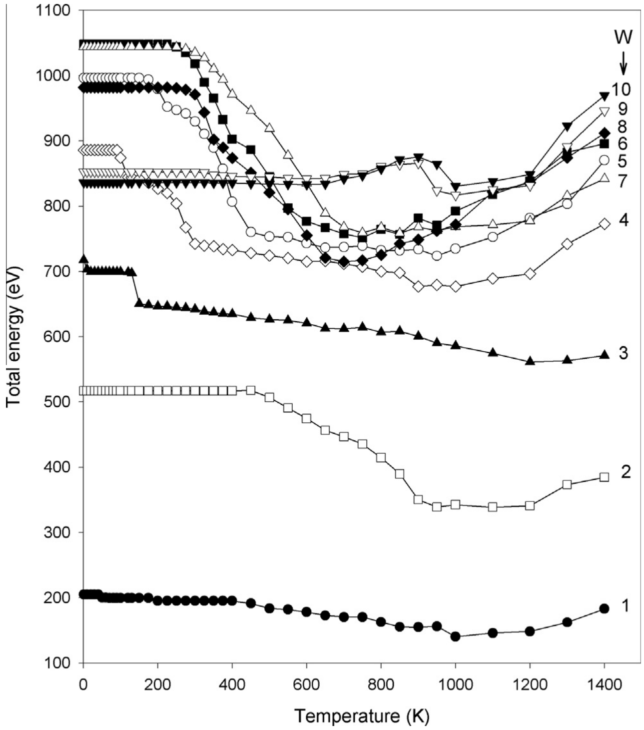

Fig. 2. Total energy (in eV) as a function of temperature for Ag nanoframes with width *W*.

of these structures to be much lower than that of the bulk material. Here, the terms "melting temperature" are used in a very approximate way, representing the temperature at which the energy of the solid rises due to disorder leading to the evaporation of some atoms. That is the case for $W = 2$, where the reduction in energy suddenly ends at $T = 1100$ K, once evaporation starts. Some differences are already apparent for $W = 3$, due to the fact that the surface to volume ratio in the sides (as well as in the corners) of the nanoframe decreases rapidly as the thickness of the sides increases. A minor decrease in energy is already apparent below room temperature, due to minor deformation of the corners and weakening of the sides. This process accelerates for $600\ \text{K} < T < 900\ \text{K}$ for BANN simulations, which could be taken as a good indication of what is to be expected experimentally. No sides are actually broken until $T = 900$ K, but numerous atoms migrate to the corners, inducing faceting. Evaporation is again present, but at a slightly higher temperature than in the $W = 2$ case, indicating the growing size (808 atoms) and stability of the now isolated corner clusters. The $W = 4$ case (1312 atoms) hints at changes in behavior due to the increasing thickness of the sides. While the processes (i.e., deformation of the corners, weakening of the sides) are essentially similar, they occur at higher temperatures than in the $W = 3$ case. Breakdown of the sides starts now at $T = 1000$ K. Once it starts, the consolidation of the corner clusters is quick and complete, with a rapid evolution towards perfectly faceted nanoclusters.

The case $W = 5$ (1848 atoms) is the first for which the sides remain whole for all temperatures in spite of an overall decrease in width and increased deformation at the center of the sides. By $T = 900$ K, the nanostructure adopts its final form, with largely faceted corners and weak (narrow) sides. Evaporation takes over above $T = 1000$ K. The case $W = 6$ (2376 atoms) shows reinforcement of the evolution seen in the $W = 5$ case, but diffusion along the smaller internal surface of the structure leads to slower debilitation of the sides, with the overall nanoframe behaving more collectively, as a single unit. For this width, the difference between corner and side sites is blurred, so no particular region of the cell provides an energetically distinct advantage.

By $W = 7$ (2840 atoms), the transition to a different type of regime is clear. In this case, the internal void is very small, and while the characteristic temperatures remain nearly the same as in previous cases (i.e., below room temperature for the onset of deformation and $T = 900$ K for the onset of evaporation), the process now favors the filling of the internal gap and the formation of a compact single nanoparticle, with no remnants of the sides or any other feature characterizing the initial nanoframe. Similar conclusions can be drawn for the $W = 8$ (3200 atoms) and $W = 9$ (3400 atoms) cases, where the formation of a single nanocluster is the immediate result of any atomic migration triggered by the rising temperature. Due to the smaller surface to volume ratio for the single cluster, the lattice parameter tends to be larger than that of the smaller clusters that originate from the corner sites in smaller nanoframes.

Summarizing, all nanoframes in this example follow the same path: (1) stability below room temperature, (2) onset of surface diffusion towards the high surface energy sites at or below room temperature, (3) ensuing deformation of the sides with bulking and faceting of the corners, (4) breakdown of the sides and transition to smaller clusters (for $W < 6$) or collective faceting and nucleation of a bigger nanoparticle (for $W > 6$) at $T = 900$ K, and (5) evaporation for temperatures lower than the melting temperature of the bulk material.

Simulations using the MCAS algorithm yield similar behavior in terms of trends, but quite different in terms of the temperature at which each process starts or ends, as it is to be expected due to the unrestricted diffusion implicit in the algorithm. It is, however, a good depiction of what the cell would look like should the exchange process have no such constraint. It could be said that while BANN depicts what all atoms tend to do in an experimental situation, MCAS gives a clearer picture of how atoms behave if they are free of any restriction. To illustrate this point, Fig. 3 shows some intermediate stages of the MCAS simulation results for Ag nanoframes with $W = 3$ and 7 cases for $N = 10$, and the $W = 13$ and 8 cases for $N = 20$, highlighting the effect of the processes described above.

Not surprisingly, the results for Au nanoframes are generally similar to those found for Ag. The main difference is a slightly higher resistance to all of the processes present in the Ag case, with slightly higher temperatures for the onset of the characteristic low temperature processes (migration, faceting, thinner sides for small *W*, clustering for large *W*), and a clear transition from between regimes (breakdown into several clusters against coalescence into a single nanoparticle) for $W > 6$. To a certain extent, it can be said that this type of differences are somewhat proportional to the small gap in the values of the melting temperature for the corresponding solids.

Much more noticeable differences can be seen in the case of Pt nanoframes. All initial structures remain practically unchanged up to high temperatures ($T \sim 900$ K), with little or any hint of any of the processes detailed above for the Ag case, found also in the Au case. This is more remarkable in frames with high *W*, which remain stable up to $T = 1600$ K. The critical width ($W = 6$) observed in Ag and Au nanoframes is not present in the Pt case. It is only in MCAS simulations that the underlying trend can be seen: high *W* nanoframes, with negligible changes in shape, tend to form a single nanoparticle with many vacancies, indicating that the low surface energy of these clusters offsets the tendency to coalesce into a solid cluster. It can be concluded that the only relevant differences between Ag, Au, and Pt are the temperatures for which each behavior is observed. This is illustrated in Fig. 4, where MCAS and BANN results for $N = 10$ and $W = 7$ for Ag, Au, and Pt are shown. The MCAS

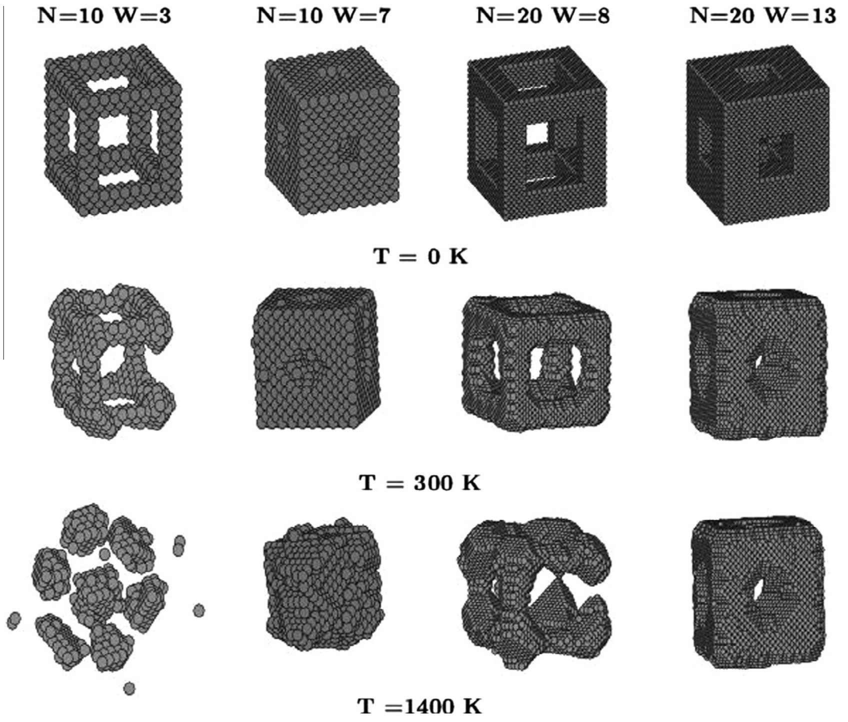

Fig. 3. Intermediate states of the MCAS computational Ag cell for (left column) $N = 10$ and $W = 3$, (center column) $N = 10$ and $W = 7$, (center column) $N = 20$ and $W = 8$ and (right column) $N = 20$, $W = 13$, for (top row) $T = 0$ K, (center row) $T = 300$ K, and (bottom row) $T = 1400$ K.

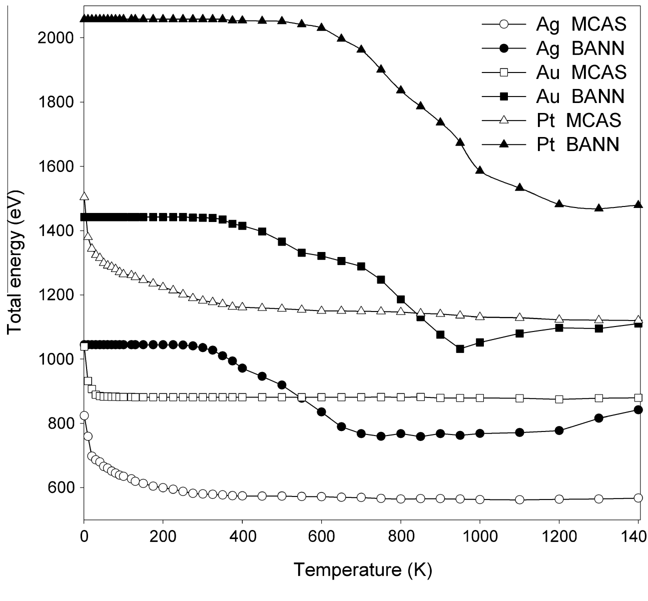

Fig. 4. Total energy (in eV) as a function of temperature for Ag, Au, and Pt nanoframes with $N = 10$ and $W = 7$, as obtained from MCAS and BANN simulations.

results (open symbols), due to what can be understood as infinite diffusion, settle rapidly into their final state, while the corresponding BANN results highlight the process of atomic migration with increasing temperature, as the nanocage evolves from its initial to final form. Similar features to the BANN curves shown in Fig. 2 can be seen, although the differences between Ag, Au, and Pt are now apparent.

As discussed above, the results of the simulations reveal two distinct behaviors depending on their original shape and size. Nanoframes with thin sides ($W \ll N$) tend to break into smaller clusters generated from the migration of side atoms to the corners, while those with thicker sides tend to coalesce and form a large particle. Clearly, the surface to volume ratio is higher for the corners than for the sides, especially for small values of W, triggering a migration of side atoms to the corners, which are more bulk-like. Conversely, for large values of W, the sides become shorter (and stronger) and the internal void much smaller, reversing the trend and leading the particle to behave as a porous bulk structure.

In spite of the complexity of this problem, simple guidelines for the description of the observed features can be obtained by simply counting the number of side and corner atoms for different values of N (number of atoms from corner to corner) and the side width W. Doing so yields a simple expression for the number of corner atoms, n_c, as an increasing function of W, given by

$$n_c = 4\left(W^3 + n_0\right) \tag{2}$$

where $n_0 = 0$ or 1 for even or odd values of W, respectively. However, the corresponding expression for the number of side atoms, n_S, given by

$$n_S = 6W^2(2N-1) - 12W^3 + d \tag{3}$$

where $d = 0$ when W is even and $d = -6$ when W is odd, exhibits a single maximum for even or odd values of W when

$$W_{\max} = \frac{2N-1}{3} \tag{4}$$

This indicates the existence of a critical value of W (for a given N) for which the number of side atoms has a maximum: below this value, side atoms outnumber corner atoms, while the opposite is true beyond the maximum. This, manifested in the behavior of the total energy shown in Fig. 2, is valid as well for Au and Pt although, as mentioned above, such processes occur at different temperatures for all three elements. This simple rule predicts a critical value for W between 6 and 7 for the $N = 10$ case which is clearly supported by the results of the simulations. Fig. 3 illustrates this behavior. The two cases shown for $N = 10$ correspond to

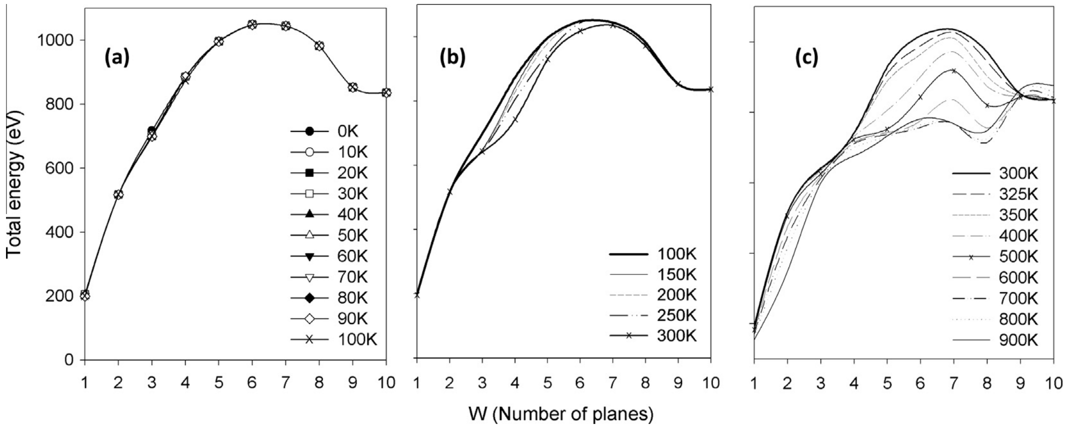

Fig. 5. Total energy (in eV) as a function of width (W) for different values of the temperature T (in K) for Ag. (a) $0 \leqslant T \leqslant 100$, (b) $100 \leqslant T \leqslant 300$, and (c) $300 \leqslant T \leqslant 900$.

widths below and above the critical value predicted by W_{max}. In the $W = 3$ case, the sides eventually disappear forming bulk-like nanoclusters from the remnants of the corners, while the $W = 7$ case shows the implosion that characterizes the high W cases. The last column shows the evolution of the nanoframe (for $N = 20$, 22,984 atoms) for the exact W_{max} value. In this case, both trends are present, manifested by a slight deformation of the sides and an overall tendency towards implosion.

These two regimes can also be seen in the evolution of the total energy (see Fig. 2). However, clearer features emerge when plotting the total energy as a function of width, $E(W)$, for different temperatures, as shown in Fig. 5. As Fig. 2 shows, not much happens below room temperature. This is reflected in Fig. 5a, which shows nearly identical curves for all values of T between 0 and 100 K. The only distinctive feature is that all curves display a maximum slightly to the right of $W = 6$. Minor changes can be seen in the range $100 \leqslant T \leqslant 300$ K (Fig. 5b), illustrating the different values for which the total energy decreases in Fig. 2. Not surprisingly, the only noticeable changes are in nanoframes with small values of W, representing the fact that in these cases there is a rapid degradation of the sides of the frame.

Above room temperature, major changes take place, as can also be seen in Fig. 5c. The single maximum for $E(W)$ for $T < 300$ K persists at higher temperatures, but the curves deform to either side of this maximum showing the formation of a shallow minimum for lower widths, and a much deeper one for higher widths. This could be interpreted as a measure of the stability of the two different behaviors/trends seen in Fig. 3. For low W, once the frame disintegrates, several clusters are generated but they are still unstable, due to the slow process of faceting and reconstruction of the resulting nanoclusters. For high W, a single nanocluster forms which, due to its smaller surface to volume ratio, stabilizes more rapidly. The values of W around the critical value continue to exhibit an energy barrier between these two regimes. Fig. 5c also reaffirms the concept that the critical range of temperatures (almost independently of width) for the transition from the explosive (several small clusters) to implosive (one large cluster) regime is in the range $T = 700–800$ K, which could be considered as an approximate value for the 'melting temperature' of Ag nanoframes. A similar range is valid for Au nanoframes, and a much higher temperature range (1100–1200 K) for Pt can be also taken as approximate values for such transition.

4. Conclusions

A modeling approach, using Monte Carlo–Metropolis simulations and the BFS method for the energetics for the study of the behavior of nanoframes, shows potential for providing information on this type of structures and establish general guidelines on their evolution with temperature and their structural properties. The results of the simulations reveal two distinct behaviors: nanoframes with thin sides ($W \ll N$) tend to break into smaller clusters generated from the migration of side atoms to the corners, while those with thicker sides tend to collapse onto their own internal void and form a large particle. The critical value of the width, W, at which the transition between regimes occurs can be calculated through a simple counting rule that relates the values of W and N with the critical width, W_{max}, via a simple expression valid for any atomic species. The onset of evaporation and the subsequent increase in energy is in the range of $T = 700–800$ K for Ag and Au nanoframes and much higher (1100–1200 K) for Pt, substantially lower than the known bulk values for the melting temperature.

However, in spite of the useful information that can be extracted from this initial modeling attempt, most nanoframes developed experimentally can hardly be considered monoatomic, and in this sense it is important to point out that proper doping of otherwise pure frames with other elements could strongly affect the final evolution with temperature and its structural properties, as outlined in this paper. A downselection of possible combinations done by means of the present modeling technique has the potential of providing the necessary information (in terms of composition and concentration) needed to achieve the desired nanoframe with well-defined properties. Therefore, future work will concentrate on binary nanoframes [22] and while generally the same behavior could be expected, the interaction between different atomic species should introduce changes that arise from segregation or ordering trends.

Acknowledgment

Fruitful discussions with N. Bozzolo are gratefully acknowledged.

References

[1] J. Hu, M. Chen, X.S. Fang, L.M. Wu, Chem. Soc. Rev. 40 (2011) 5472.
[2] F. Zhang, Y.F. Shi, X.H. Sun, D.Y. Zhao, G.D. Stucky, Chem. Mater. 21 (2009) 5237.
[3] J. Liu, S.Z. Qiao, S.B. Hartono, G.Q. Lu, Angew. Chem. Int. Ed. 49 (2010) 4981.
[4] J. Liu, S.B. Hartono, Y.G. Jin, Z. Li, G.Q. Lu, S.Z. Qiao, J. Mater. Chem. 20 (2010) 4595.
[5] Z. Sun, J.H. Kim, Y. Zhao, F. Bijarbooneh, V. Malgras, Y. Lee, Y.M. Kang, S.X. Dou, J. Am. Chem. Soc. 133 (2011) 19314.
[6] U. Kreibig, M. Vollmer, Optical Properties of Metal Clusters Springer Series in Materials Science, vol. 25, Springer, Berlin, 1995, p. 125.
[7] F. Bai, Z.C. Sun, H.M. Wu, R.E. Haddad, X.Y. Xiao, H.Y. Fan, Nano Lett. 11 (2011) 3759.

[8] Z.M. Peng, J.B. Wu, H. Yang, Chem. Mater. 22 (2010) 1098.
[9] J.X. Wang, C. Ma, Y.M. Choi, D. Su, Y.M. Zhu, P. Liu, R. Si, M.B. Vukmirovic, Y. Zhang, R.R. Adzic, J. Am. Chem. Soc. 133 (2011) 13551.
[10] I. Brigger, C. Dubernet, P. Couvreur, Adv. Drug Deliv. Rev. 54 (2002) 631.
[11] X. Huang, I. El-Sayed, W. Qian, M.A. El-Sayed, J. Am. Chem. Soc. 128 (2006) 2115.
[12] J. Hainfeld, D. Slatkin, H. Smilowitz, Phys. Med. Biol. 49 (2004) N309.
[13] D. Wu, X. Zhang, P. Liu, L. Zhang, F. Fan, M. Guo, Curr. Nanosci. 7 (2011) 110.
[14] C. Murphy, A. Gole, J. Stone, P. Sisco, A. Alkilany, E. Goldsmith, S. Baxter, Acc. Chem. Res. 41 (2008) 1721.
[15] X.D. Zhang, H.Y. Wu, Int. J. Nanomed. 5 (2010) 771.
[16] X.D. Zhang, M.L. Guo, H.Y. Wu, Y.M. Sun, Y.Q. Ding, X. Feng, L.A. Zhang, Int. J. Nanomed. 4 (2009) 165.
[17] Y.G. Sun, Y.N. Xia, Science 298 (2002) 2176.
[18] X. Lu, L. Au, J. McLellan, Z-Y. Li, M. Marquez, Y. Xia, Nano Lett. 7 (2007) 1764.
[19] L. Au, Y. Chen, F. Zhou, P.H.C. Camargo, B. Lim, Z-Y. Li, D.S. Ginger, Y. Xia, Nano Res. 1 (2008) 441.
[20] S.E. Skrabalak, J. Chen, Y. Sun, X. Lu, L. Au, L.M. Cobley, Y. Xia, Acc. Chem. Res. 41 (2008) 1587.
[21] M. Rycenga, Z. Wang, E. Gordon, C. Cobley, A.G. Schwartz, C.S. Lo, Y. Xia, Angew. Chem. Int. Ed. Engl. 48 (2009) 9924.
[22] M.A. Mahmoud, M.A. El-Sayed, Langmuir 28 (2012) 4051.
[23] R. Wu, K. Qing-Cheng, F. Chenglin, L. Shi-Qin, Y. Cui, L. Jian-Yu, C. Yongxiang, H. Jian-Qiang, RSC Adv. 3 (2013) 12577.
[24] G.D. Moon, S.W. Choi, X. Cai, W. Li, E.C. Cho, U. Jeong, L.V. Wang, Y. Xia, J. Am. Chem. Soc. 133 (2011) 4762.
[25] J. Chen, B. Wiley, Z.Y. Li, D. Campbell, F. Saeki, H. Cang, Y. Xia, Adv. Mater. 17 (2005) 2255.
[26] P.K. Jain, X. Huang, I.H. El-Sayed, M.A. El-Sayed, Acc. Chem. Res. 41 (2008) 1578.
[27] M.A. Mahmoud, R. Narayanan, M.A. El-Sayed, Acc. Chem. Res. 46 (2013) 1795.
[28] H. Zhang, M. Jin, H. Liu, J. Wang, M.J. Kim, D. Yang, Z. Xie, J. Liu, Y. Xia, ACS Nano 5 (2011) 8212.
[29] C. Ji, H.S. Park, Nanotechnology 18 (2007) 115707.
[30] Q. Shu, Y. Yang, Y.T. Zhai, D.Y. Sun, H.J. Xianga, X.G. Gong, Nanoscale 4 (2012) 6307.
[31] J.W. Kang, J.J. Seo, H.J. Hwang, J. Phys.: Condens. Matter 14 (2002) 8997.
[32] A.N. Enyashin, A.L. Ivanovskii, J. Mol. Struct.: THEOCHEM 822 (2007) 28.
[33] F. Delogu, J. Phys. Chem. C 112 (2008) 11135.
[34] S. Jiang, H. Zhang, Y. Zheng, Z. Chen, J. Phys. D: Appl. Phys. 42 (2009) 135408.
[35] S. Jiang, Y. Zhang, Y. Gan, Z. Chen, H.S. Peng, J. Phys. D: Appl. Phys. 46 (2013) 335302.
[36] F. Delogu, J. Phys. Chem. A 112 (2008) 2863.
[37] G. Bozzolo, J. Ferrante, J.R. Smith, Phys. Rev. B 45 (1992) 493.
[38] G. Bozzolo, J.E. Garcés, The chemical physics of solid surfaces, in: D.P. Woodruff (Ed.), Surface Alloys and Alloy Surfaces, vol. 10, Elsevier, New York, 2002, p. 30.
[39] A. Wilson, G. Bozzolo, R.D. Noebe, J.M. Howe, Acta Mater. 50 (2002) 2787.
[40] G. Bozzolo, J.E. Garcés, R.D. Noebe, D. Farías, Nanotechnology 14 (2003) 939.
[41] C. Pint, G. Bozzolo, R. Hauge, Nanotechnology 19 (2008) 405704.
[42] F. Negreiros Ribeiro, E. Avellar Soares, V.E. de Carvalho, G. Bozzolo, Phys. Rev. B 76 (2007) 245432.
[43] A. Zink, G. Bozzolo, H.O. Mosca, Int. J. Nanosci. 11 (2012) 1250011.
[44] D.C. Kara, M.S. Drexel, G. Bozzolo, H.O. Mosca, Int. J. Nanosci. 9 (2010) 413.
[45] J. Smith, T. Perry, A. Banerjea, J. Ferrante, G. Bozzolo, Phys. Rev. B 44 (1991) 6444.
[46] P. Blaha, K. Schwarz, G.K.H. Madsen, D. Kvasnicka, J. Luitz, WIEN2K, in: K. Schwarz (Ed.), An Augmented Plane Wave + Local Orbitals Program for Calculating Crystal Properties, Techn. Universität Wien, Wien, 2001.
[47] G. Bozzolo, J. Khalil, R.D. Noebe, Comput. Mater. Sci. 24 (2002) 457.
[48] G. Bozzolo, R.D. Noebe, J. Ferrante, C. Amador, J. Comput. Aided Mater. Des. 6 (1999) 1.